

A Chandra Study of Radial Temperature Profiles of the Intra-Cluster Medium in 50 Galaxy Clusters

Zhenghao Zhu¹, Haiguang Xu^{1,2}, Jingying Wang⁴, Junhua Gu⁴, Weitian Li¹, Dan Hu¹,
Chenhao Zhang¹, Liyi Gu⁵, Tao An⁶, Chengze Liu¹, Zhongli Zhang⁷, Jie Zhu³ AND
Xiang-Ping Wu⁴

Received _____; accepted _____

¹Department of Physics and Astronomy, Shanghai Jiao Tong University, 800 Dongchuan Road, Minhang, Shanghai 200240, China; email: clsn@sjtu.edu.cn, hgxu@sjtu.edu.cn;

²IFSA Collaborative Innovation Center, Shanghai Jiao Tong University, 800 Dongchuan Road, Minhang, Shanghai 200240, China;

³Department of Electronic Engineering, Shanghai Jiao Tong University, 800 Dongchuan Road, Minhang, Shanghai 200240, China;

⁴National Astronomical Observatories, Chinese Academy of Sciences, 20A Datun Road, Beijing 100012, China;

⁵SRON Netherlands Institute for Space Research, Sorbonnelaan 2, 3584 CA Utrecht, the Netherlands;

⁶Shanghai Astronomical Observatory, Chinese Academy of Sciences, 80 Nandan Road, Shanghai 200030, China;

⁷Max Planck Institute for Astrophysics, Karl-Schwarzschild-Str. 1, Postfach 1317, D-85741 Garching, Germany.

ABSTRACT

In order to investigate the spatial distribution of the ICM temperature in galaxy clusters in a quantitative way and probe the physics behind, we analyze the X-ray spectra of a sample of 50 galaxy clusters, which were observed with the *Chandra* ACIS instrument in the past 15 years, and measure the radial temperature profiles out to $0.45r_{500}$. We construct a physical model that takes into account the effects of gravitational heating, thermal history (such as radiative cooling, AGN feedback, and thermal conduction) and work done via gas compression, and use it to fit the observed temperature profiles by running Bayesian regressions. The results show that in all cases our model provides an acceptable fit at the 68% confidence level. To further validate this model we select nine clusters that have been observed with both *Chandra* (out to $\gtrsim 0.3r_{500}$) and *Suzaku* (out to $\gtrsim 1.5r_{500}$), fit their *Chandra* spectra with our model, and compare the extrapolation of the best-fits with the *Suzaku* measurements. We find that the model profiles agree with the *Suzaku* results very well in seven clusters. In the rest two clusters the difference between the model and observation is possibly caused by local thermal substructures. Our study also implies that for most of the clusters the assumption of hydrostatic equilibrium is safe out to at least $0.5r_{500}$, and the non-gravitational interactions between dark matter and its luminous counterpart is consistent with zero.

Subject headings: galaxies: clusters: general — galaxies: clusters: intracluster medium — X-rays: galaxies: clusters.

1. INTRODUCTION

Galaxy clusters are the most massive virialized systems in our Universe, whose gravitational potential wells are dominated by dark matter that accounts for up to about 90% of the total mass. Except for the gravity, however, the interaction between dark matter and its luminous counterparts is extraordinary small (e.g., Munoz et al. 2015), thus nearly all of the contemporary studies of clusters have been performed via observing the luminous components, i.e., highly ionized intra-cluster medium (ICM), stellar component, as well as various warm and cool gases, with an emphasis in the X-ray band since the ICM overwhelms other luminous components in mass by a factor of a few (e.g., Makishima et al. 2001 and references therein). The temperature of the ICM, which can be directly measured in spaceborne observations, is a fundamental quantity that can be used to either characterize the thermodynamic status of the ICM, or calculate the total gravitating mass and various X-ray scaling relations (Xu et al. 2001), or interpret the Sunyaev-Zeldovich (SZ) effect (Lin et al. 2015). It also provides us with valuable information about astrophysical processes such as AGN feedback, thermal conduction, merger, and radiative cooling. Moreover, the knowledge about the ICM temperature also helps constrain the parameters of our cosmological models (e.g., Kravtsov & Borgani 2012).

Apparently, in order to carry out physical study of a cluster, an accurate determination of the ICM temperature and its spatial variation within a significant part of the virial radius is crucial. As a standard procedure, after the best-fit gas temperatures obtained for the spectra extracted from a set of adjacent annular or pie regions, both interpolation within each of these regions and extrapolation to larger radii are necessary to obtain a smooth gas temperature profile due to the limited capacity of today’s instruments. This invokes a relatively simple and, if possible, universal analytic expression for the temperature profile. As one of the first attempts, Allen et al. (2001) analyzed the *Chandra* pointing observations of

seven relaxed clusters, which are located within a redshift range of $0.10 \sim 0.46$, and proposed a 4-parameter empirical profile for the radial distribution of gas temperature. Using *Chandra* and *XMM-Newton* data, different but similar temperature profiles were introduced by, e.g., Vikhlinin et al. (2006) to calculate the total gravitating mass of 13 low-redshift relaxed clusters, Zhang et al. (2006) to determine the X-ray scaling relations of 14 distant X-ray luminosity, and Ascasibar et al. (2006) to probe the origin of the cold fronts in the ICM. These profiles and their analogs were evaluated and compared with each other by Gastaldello et al. (2007).

Despite the successful applications of the empirical temperature profiles listed above, the following two questions may still be raised: what is the intrinsic physics behind these empirical profiles and how reliable it is when we extrapolate these profiles out to the skirt region of a cluster? In this work, we address this issue by analyzing the X-ray data of a sample of 50 galaxy clusters ($z = 0.05 \sim 0.46$), which are drawn from *Chandra*'s 15-year archive, and fitting the observed radial temperature profiles with a physical model that takes into account the effects of gravitational heating during the halo collapse, thermal history (such as radiative cooling, AGN feedback, and thermal conduction), and work done via gas compression. In §2 and §3, we describe the sample selection criteria and data analysis, respectively. In §4, we introduce the model and use it to fit the observed temperature profiles. In §5, we select nine clusters that have been observed with *Suzaku* out to or even beyond $1.5r_{500}$ (r_{500} is defined as the radius within which the mean enclosed mass density of the target is 500 times the critical density of the Universe at the target's redshift), extrapolate the best-fit *Chandra* temperature profiles obtained with our new model to $1.5r_{500}$ and compare the results with the *Suzaku* measurements. We also discuss the applicability of the hydrostatic equilibrium assumption and the constraint on the non-gravitational interaction between dark and luminous matters. In §6, we summarize our results. Throughout the work we adopt a flat Λ CDM cosmology with density parameters $\Omega_m = 0.27$ and $\Omega_\Lambda = 0.73$, and Hubble

constant $H_0 = 71 \text{ km s}^{-1} \text{ Mpc}^{-1}$. Unless stated otherwise, we used the solar abundance standards of Grevesse & Sauval (1998) and quote errors at 68% confidence level.

2. SAMPLE SELECTION AND DATA PREPARATION

In order to measure and characterize the spatial distribution of gas temperature in a galaxy cluster, both a high signal-to-noise ratio (SNR) and a balance between sufficient angular resolution and complete detector coverage of the target are necessary. To this end, we constructed our *Chandra* sample by applying the following selection criteria: (1) a large part of the target out to at least $0.45r_{500}$ is fully or nearly fully covered by either the S3 CCD or the I0-3 CCDs of the *Chandra* Advanced CCD Imaging Spectrometer (ACIS) instrument, (2) the number of photons contained inside $0.45r_{500}$ is no less than 12500 cts, and (3) the target exhibits a relatively regular appearance and possesses no significant substructures. As a result we drew 50 clusters from the *Chandra* archive, whose redshifts, average temperatures (see §3.3), and X-ray luminosities span ranges of $0.05 - 0.46$, $3 - 16 \text{ keV}$, and $7 \times 10^{43} - 5 \times 10^{45} \text{ erg s}^{-1}$, respectively (Table 1).

For each observation, we followed the standard *Chandra* data processing procedure to prepare the data by using CIAO v4.4 and CALDB v4.4.8, by starting with the ACIS level 1 event files, which were collected with a frame time of 3.2 s telemetered in the FAINT or VFaint mode. We removed all bad pixels and columns, as well as events with *ASCA* grades 1, 5, and 7 and carried out corrections for the gain, charge transfer inefficiency (for the observations performed after January 30, 2000), astrometry, and cosmic ray afterglow. By examining the light curves extracted in $0.5 - 12 \text{ keV}$ from source-free regions or regions less contaminated by the sources on the S3 or I0-3 CCDs, we identified and excluded time intervals contaminated by occasional particle background flares during which the count rate rises to $> 120\%$ of the mean value. When available, data of S1 CCD were also analyzed to

cross check the determination of the contaminated intervals. All the point sources detected beyond the 3σ threshold in the ACIS images with CIAO tools **celldetect** and **wavedetect** have been masked in the analysis.

3. DATA ANALYSIS AND RESULTS

3.1. Background

In order to construct the local background of each observation, we extract the spectrum from one or several separate boundary regions on the S3 CCD or I0-3 CCDs, where the thermal emission of the cluster is relatively weak but usually cannot be neglected, and fit the extracted spectrum in $0.4 - 12$ keV (e.g., Sun et al. 2009; Vikhlinin et al. 2005) with a model that consists of an absorbed thermal APEC component (the absorption is fixed to the Galactic value given in Kalberla et al. 2005; Dickey & Lockman 1990, and the abundance is set to $0.3 Z_{\odot}$ if it is not well constrained; e.g., Panagoulia et al. 2014), an absorbed power-law component for the Cosmic X-ray Background (CXB; $\Gamma = 1.4$; e.g., Mushotzky et al. 2000; Carter & Read 2007), a Galactic emission component (two APEC components with $T_X = 0.2$ and 0.08 keV, respectively; e.g., Gu et al. 2012; Humphrey & Buote 2006), and a particle-induced hard component calculated from the corresponding *Chandra* blanksky templates provided by the *Chandra* Science Center. The background template employed in this work, i.e., Galactic + CXB + particle components, can be determined after the best-fit is achieved. When available, we also cross checked our background templates with the $0.2 - 2$ keV *ROSAT* All-Sky Survey (RASS) diffuse background maps, where the particle component is minor, and obtained consistent results. In order to approximate the field-to-field variation of the Galactic and CXB background components in each observation, in the imaging and spectral analysis that follows we estimate the model parameter errors by taking into account both statistical and systematic uncertainties (10%; Kushino et al. 2002) in the background.

3.2. Radial Temperature Distributions of the ICM

In order to calculate the azimuthally averaged gas temperature distributions of the sample clusters, for each observation, we extract the *Chandra* ACIS spectra from 5 – 7 concentric annuli, which are all centered on the X-ray peak and cover the $\simeq 0.45r_{500}$. The width of each annulus is determined in such a way that a minimal photon count of 2500 cts in 0.7 – 7 keV is guaranteed, while in the outmost annulus the condition that the photon count is at least twice the background is simultaneously satisfied. We perform the spectral model fittings by employing the X-ray spectral fitting package XSPEC v12.8.2 (Arnaud 1996), and limit the fittings in 0.7 – 7 keV to minimize the effect of the instrumental background at higher energies and the calibration uncertainties at lower energies.

In the spectral analysis we use the XSPEC model PROJCT to evaluate the influence of the outer spherical shells on the inner ones, and fit the deprojected spectra by applying the optically thin thermal plasma model APEC (Smith et al. 2001), which is absorbed by the foreground photoelectric absorption model WABS. For each cluster, the column density N_{H} of the WABS model is fixed to the corresponding Galactic value (Kalberla et al. 2005; Dickey & Lockman 1990), and the redshift of the APEC component is fixed to the value given in literature, which can be found in the NASA Extragalactic Database (NED). Whenever the metal abundance of the hot gas is not well constrained, we fix it to $0.3 Z_{\odot}$ (e.g., Panagoulia et al. 2014). For the innermost annulus, we also attempt to add an additional absorbed APEC component to represent the possible cooler phase gas, the origin of which is often ascribed to the central dominating galaxy (e.g., Makishima et al. 2001). When the F-test shows that the fitting is improved at the 90% confidence level, we choose to use the two-phase gas model and define the temperature of the intergalactic gas as that of the hot phase. The obtained gas temperature distributions are shown in Figure 1, along with the errors calculated at 68 % confidences level.

3.3. Spatial Distributions of Gas Density, Gas Entropy and Total Gravitational Mass

We extract the X-ray surface brightness profiles $S_X(R)$ (R is the two dimensional radius) in $0.7 - 7$ keV from a set of concentric annular bins that are all centered at the X-ray peak of the gas halo, and correct them by applying the exposure maps to remove the effect of vignetting and exposure time fluctuations. The exposure maps are created using the spectral weights calculated for an incident thermal gas spectrum that possesses the same average temperature and metal abundance as the cluster (§3.2). We assume both hydrodynamic equilibrium and spherical symmetry so that the three-dimensional spatial distribution of the electron density n_e follows either the β -model,

$$n_e(r) = n_0[1 + (\frac{r}{r_c})^2]^{-3\beta/2}, \quad (1)$$

or the double- β model

$$n_e(r) = n_{0,1}[1 + (\frac{r}{r_{c,1}})^2]^{-3\beta_1/2} + n_{0,2}[1 + (\frac{r}{r_{c,2}})^2]^{-3\beta_2/2} \quad (2)$$

when a significant central surface brightness excess is detected in the inner regions (e.g., Makishima et al. 2001), where r_c and β are defined as the core radius and slope parameter, respectively. Given the gas density distribution profiles and the radial distributions of gas temperature and metal abundance obtained by running cubic spline interpolation to the best-fit temperatures and abundances (§3.2), we model the extracted X-ray surface brightness profile as

$$S_X(R) = \int_R^\infty \Lambda(T, A) n_e n_p(r) \frac{r dr}{\sqrt{r^2 - R^2}} + S_{\text{bkg}}, \quad (3)$$

where S_{bkg} is the diffuse X-ray background, and $\Lambda(T, A)$ is the cooling function. The electron density $n_e(r)$ and gas entropy $K(r) = T(r)n_e(r)^{-2/3}$ are determined when the best-fit to the observed surface brightness profile is achieved by minimizing the χ^2 . Note that the entropy

$K(r)$ is the customary “entropy” used in the X-ray cluster field, in comparison with the classical definition $S \propto \Delta K/K$ (see Voit 2005a for a review).

The total gravitating mass of the cluster is calculated as

$$M(< r) = -\frac{r^2 k_b T_X}{G \mu m_p} \left[\frac{1}{T_X} \frac{dT_X}{dr} + \frac{1}{n_e} \frac{dn_e}{dr} \right], \quad (4)$$

where $\mu = 0.61$ is the mean molecular weight per hydrogen atom, k_b is the Boltzmann constant, and m_p is the proton mass. In order to extrapolate the obtained mass profile out to the virial radius, we employ the NFW model (Navarro et al. 1996)

$$\rho(r) = \frac{\rho_0}{(1 + r/r_s)^2 r/r_s}, \quad (5)$$

where $\rho(r)$ is the density of the total gravitational mass, ρ_0 and r_s are free parameters in the NFW model. The average temperatures of the clusters are calculated by fitting the spectra extracted in $0.2 - 0.5 r_{500}$, using the same method described in §3.2. We show the physical properties of clusters in Table 2.

4. MODELING AND FITTING OF THE OBSERVED TEMPERATURE PROFILES

4.1. Effects of Gravity and Non-gravitational Processes

In this section we attempt to introduce an universal profile to describe the observed gas temperature profiles by taking account the effects of both gravity and non-gravitational processes, the latter includes the polytropic compression and thermal history (such as radiative cooling, AGN feedback, and thermal conduction) of the gas. For a small test gas element, whose position, mass, and particle number density are r , m^* , and n^* , respectively, we mark the gravitational energy released during the halo collapse as ΔE_G , and the energy transferred to it by the non-gravitational processes as ΔE_{NG} . Thus the total energy available

to increase the internal energy of the test gas element is expressed as

$$E_{\text{total}}(r) = \Delta E_{\text{G}}(r) + \Delta E_{\text{NG}}(r). \quad (6)$$

Energy Released in the Gravitational Collapse

First let us consider the gravitational energy release of the test gas element during the collapse of the cluster. As in §3.3, we assume that at present time the gravitational potential of the system can be described by the NFW model (Navarro et al. 1996). Thus when the test gas element falls from infinity to its present position r , the gravitational energy release is

$$\Delta E_{\text{G}} = \frac{G \int_0^r \rho(x) 4\pi x^2 m^* dx}{r} + \int_r^\infty \frac{G \rho(x) 4\pi x^2 m^* dx}{x} = \frac{G \rho_0 4\pi m^* r_s^3}{r} \ln \left(\frac{r + r_s}{r_s} \right), \quad (7)$$

where G is the gravitational constant. This equation denotes the upper limit on the thermal energy increase that can be caused by the gravitational collapse.

Contributions of the Non-gravitational Processes

Next we investigate the energy transferred to the test gas element by non-gravitational processes. As a simple and reasonable assumption, this part of energy is attributed to the work done by gas compression (ΔE_{work}) and the net heating supply determined by the thermal history which typically involves radiative cooling, AGN heating, and thermal conduction ($\Delta E_{\text{heating}}$), i.e., $\Delta E_{\text{NG}} = \Delta E_{\text{work}} + \Delta E_{\text{heating}}$. Assuming that ideal gas undergoing polytropic processes that is characterized by the index n during the halo collapse, the state of equations can be written as:

$$p^* V^* = \nu_{\text{mol}}^* \mathcal{R} T^* \quad \text{and} \quad p^* V^{*n} = \text{const}, \quad (8)$$

where p^* , V^* , and T^* are the pressure, volume and temperature of the test gas element, respectively, \mathcal{R} is the universal gas constant, and $\nu_{\text{mol}}^* = n^*/N_A$ is the mole number as N_A is

the Avogadro constant. Thus the work done by the surrounding gas during the compression is calculated by integrating p^*dV^* from the initial state 1 to the final state 2

$$\begin{aligned}\Delta E_{\text{work}} &= \int_{V_1^*}^{V_2^*} -p^*dV^* = p_2^*V_2^{*n} \int_{V_2^*}^{V_1^*} \frac{dV}{V^{*n}} = \frac{p_2^*V_2^*}{n-1} \left[1 - \left(\frac{V_2^*}{V_1^*} \right)^{n-1} \right] \\ &= \frac{1}{n-1} (p_2^*V_2^* - p_1^*V_1^*) = \frac{\nu_{\text{mol}}^* \mathcal{R}}{n-1} (T_2^* - T_1^*).\end{aligned}\tag{9}$$

Now by applying the second law of thermodynamics, we use the entropy change ΔS to estimate the amount of net non-gravitational heating as $T\Delta S$. Clearly the change of the classical entropy satisfies $\Delta S \propto \Delta K/K$, where $K = Tn_e^{-2/3}$ as defined in §3.3. Thus we obtain

$$\Delta E_{\text{heating}}(r) = C_h n^* k_b T(r) (K_{\text{obs}}(r) - K_{\text{model}}(r)) / K_{\text{obs}}(r),\tag{10}$$

where C_h is the scaling factor (Chaudhuri et al. 2012), K_{obs} is the observed entropy profile, and K_{model} is the entropy profile predicted in the hydrodynamical simulation in which only the effect of gravitational energy release is considered. In our calculation, the observed entropy profile is derived by fitting the entropy distribution given in §3.3 with an empirical model

$$K_{\text{obs}}(r) = K_1 + A_1 \times r^{\gamma_1},\tag{11}$$

where K_1 , A_1 and γ_1 are parameters constrained by observation. The model predicted entropy profile, on the other hand, is quoted from Voit et al. (2005b) as

$$K_{\text{model}}(r) = K_0 + A_0 \times r^{\gamma_0},\tag{12}$$

where K_0 , A_0 , and γ_0 are the parameters given by Eqs. 9, 10 and Figure 5 in Voit et al.

Fraction of Energy Transferred into the Thermal Form

Not all of the energy supply available in the gravitational collapse and non-gravitational processes have been transferred into the thermal energy of the test gas element, and part of them may have been mainly stored as kinetic energy. To account for this energy loss,

we introduce an efficiency factor $\eta(r)$ to represent the ratio of the energy transferred into the thermal form to the total energy supplied in both gravitational and non-gravitational processes, i.e.,

$$\eta(r) = E_{\text{thermal}}/E_{\text{total}} = \frac{3}{2}n^*k_bT(r)/E_{\text{total}} \quad (13)$$

where E_{total} is determined by Eqs. 6, 7, 9 and 10. Since $E_{\text{thermal}}/E_{\text{total}} = \bar{v}_{\text{thermal}}^2/(\bar{v}_{\text{thermal}}^2 + \bar{v}_{\text{kinetic}}^2) = P_{\text{thermal}}/P_{\text{total}} = 1 - P_{\text{kinetic}}/P_{\text{total}}$, where P_{thermal} , P_{kinetic} , and P_{total} are the thermal, kinetic, and total pressure, respectively. Using $P_{\text{kinetic}}/P_{\text{total}}$ given in Battaglia et al. (2012) we calculate the efficiency as

$$\eta(r) = 1 - \alpha_0(1+z)^{\beta_h} \left(\frac{r}{R_{500}} \right)^{n_{\text{nt}}} \left(\frac{M_{200}}{3 \times 10^{14} M_{\text{sun}}} \right)^{n_M}, \quad (14)$$

where $\alpha_0 = 0.18 \pm 0.06$, $\beta_h = 0.5$, $n_{\text{nt}} = 0.8 \pm 0.25$, and $n_M \simeq 0.2$ as calculated in Battaglia et al. (2012).

Gas Temperature Profile

Substituting Eqs. 6, 7, 9, 10, and 14 into 13, and noting that T_1^* is the effective initial temperature defined under the quasi-static assumption, which is estimated to be of the order $T_G = 2\Delta E_G/(3n^*k_b)$ and $T_2^* = T(r)$ is the observed temperature today, we obtain

$$T(r) = \frac{2\eta(r)}{3n^*k_b} \left(C_h n^* k_b T(r) \frac{K_{\text{obs}}(r) - K_{\text{model}}(r)}{K_{\text{obs}}(r)} + \frac{\nu_{\text{mol}}^* \mathcal{R}}{n-1} (T(r) - T_G) + \frac{G\rho_0 4\pi m^* r_s^3}{r} \ln \left(\frac{r+r_s}{r_s} \right) + n^* e_0 \right) \quad (15)$$

where e_0 is the average initial energy for a single particle in the gas element, which should be approximately zero. Rewriting this immediate yields the temperature profile

$$T(r) = \frac{T_0 + (1 - C_3)C_1\rho_0 r_s^3 \ln((r_s + r)/r_s)/r}{1/\eta(r) - C_3 - C_2(K_{\text{obs}}(r) - K_{\text{model}}(r))/K_{\text{obs}}(r)}, \quad (16)$$

where the temperatures are measured in keV. In this formula, $T_0 = 2e_0/3k_b$ is the initial gas temperature and is assumed to be $\simeq 0$. The parameter $C_1 = 8\pi G\mu m_p/3$, where $\mu m_p = m^*/n^* \simeq 0.61m_p$ is a fixed combination of physical constants. $C_2 = 2C_h/3$ is related to the scaling factor C_h (c.f., Eq. 10), which equals 1.5 in an isochoric process (e.g., Chaudhuri et al. 2012). $C_3 = 2/(3(n-1))$, where n is the polytropic index to be decided in the fitting. The

parameters $\eta(r)$ (c.f., Eq. 14), $K_{\text{model}}(r)$ (c.f., Eq. 12), K_{obs} , ρ_0 and rs as well as their error ranges are constrained by observations, simulations and/or scaling relations in the Bayesian model fittings (§4.2).

4.2. Fitting Method and Results

By assuming that the parameters in our model are independent, which can be considered as a good approximation in practice, we use Eq. 16 to fit the gas temperature distributions observed with *Chandra* (§3.2) by running Bayesian regressions (e.g., Andreon & Hurn 2013; Andreon 2012). Compared with chi-squared test and maximum-likelihood estimation, this approach has the advantage that it incorporates observation errors in the model meanwhile it can quantify both the intrinsic scatter and the uncertainties of the known model parameters. To be specific, we apply Bayes theorem to express the posterior probability distribution as the product of the prior distribution, which is tightly constrained by the uncertainty ranges of known model parameters (c.f., Eq. 16), and the likelihood function determined according to the error ranges of gas temperature allowed by the observation, i.e.,

$$\Pr(\text{fitted parameter}|\text{observed data}) \propto \Pr(\text{fitted parameter}) \times \Pr(\text{observed data}|\text{fitted parameter}) \quad (17)$$

and maximize it with Powell’s method (Powell 1964), which is powerful for calculating the local maximum of a continuous but complex function. When the maximum is found, the best-fit temperature profile is achieved. We plot the best-fit profiles in Figure 1, where the 68% error bands of the model computed by Monte-Carlo simulation are shown in shadow. To evaluate the goodness of the fittings, we introduce the model efficiency R_{eff} (See Nash & Sutcliffe 1970 and Engeland & Gottschalk 2002), which is defined as

$$R_{\text{eff}} = \frac{1}{N_{\text{bin}}} \sum_{i=1}^{N_{\text{bin}}} R_{\text{eff},i}, \quad \text{and}$$

$$R_{\text{eff},i} = 1 - \frac{\sum_{n=1}^{N_{\text{sim}}} (T_{i,n,\text{sim}} - T_{i,n,\text{mod}})^2}{\sum_{n=1}^{N_{\text{sim}}} (T_{i,n,\text{sim}} - T_{i,n,\text{obs}})^2}, \quad (18)$$

where N_{bin} is the bin number of the observed temperature distribution, $N_{\text{sim}} = 1000$ is the total number of Monte-Carlo simulation, and T_{sim} , T_{mod} and T_{obs} represent the simulated, model-predicted and observed temperatures, respectively. As shown in Table 2, for all of the clusters, the new profile proposed in this work gives an acceptable fit ($R_{\text{eff}} \sim 0$), although in five cases ($R_{\text{eff}} \sim -1$) one data bin deviates the from model prediction slightly (68 % confidence level). To describe the degree of the violation to the hydrostatic equilibrium, we also plot the best-fit non-thermal energy fraction $1 - \eta(r)$ as a function of radius for all clusters in Figure 2.

5. DISCUSSION

5.1. A Comparison with *Suzaku*'s Results

In order to further validate our temperature profile model we select nine galaxy clusters (Table 3), seven of which are not involved in our sample due to either a small ($< 0.45r_{500}$) field coverage or a low signal-to-noise ratio in the *Chandra* observation, calculate their gas temperature profiles with the ACIS S3 or I0-3 data, extrapolate the best-fit model profiles derived with Eq. 16 to $1.5r_{500}$, and compare the results with those measured with the *Suzaku* satellite (see references in Table 3), as shown in Figure 3. The difference between the temperatures measured with *Chandra* and *Suzaku* caused by the energy dependence of the stacked residuals ratios, (i.e., the energy-dependent difference between the effective areas of the two instruments even after careful calibrations; Schellenberger et al. 2015; Kettula et al. 2013; Nevalainen et al. 2010), has been compensated by using the data provided by

Schellenberger et al. (2015)¹.

We find that within $1.5r_{500}$ (roughly $1.0r_{200}$) of seven clusters our model profiles are in good agreement with the *Suzaku* measurements at the 68% confidence level. For A1835 the model prediction is higher than the *Suzaku* measurement in $r \gtrsim r_{500}$, where a break on the observed gas entropy distribution is detected against the theoretical power-law distribution. This is an indication of the appearance of additional cooler gas, which can be associated with contacting regions between the cluster and large-scale structure environment (Ichikawa et al. 2013). For A2029 our model underestimates the *Suzaku* temperatures in $0.13 - 0.5 r_{500}$, which might be due to substructures of the cluster.

5.2. Are the Sample Clusters in Hydrodynamic Equilibrium?

Hydrostatic equilibrium has been widely assumed in X-ray imaging spectroscopic analysis of galaxy clusters because, e.g., by adopting this assumption, the projection effect can be well restricted in measuring the X-ray mass, meanwhile the scatter of X-ray mass measurements is about a factor of two smaller than that of the lensing masses. However, both observations and simulations show that the X-ray mass measurements are generally biased low by 5 – 20% due to violation of the hydrostatic equilibrium due to mergers and bulk motions of the gas (e.g., Meneghetti et al. 2010), especially in the skirt regions. When this violation occurs, we may employ the efficiency factor $\eta(r)$ introduced in §4.1 to describe the degree of the violation as $E_{\text{non-thermal}}/E_{\text{total}} = 1 - \eta(r)$, which is typical $< 10\%$ inside $0.3r_{200}$ and increases to $\simeq 20\%$ at r_{200} (Battaglia et al. 2012). In our model fittings of the *Chandra*

¹The authors listed the *Chandra* and *XMM-Newton* measurements of gas temperature to show their difference, meanwhile it is known that the *Suzaku* and *XMM-Newton* measurements of temperature are consistent with each other in $0.7 - 7$ keV.

temperature profiles of the sample clusters (§4.2), we usually obtain $E_{\text{non-thermal}}/E_{\text{total}} \lesssim 0.12$ at small and intermediate radii, whereas $E_{\text{non-thermal}}/E_{\text{total}}$ reaches to $\simeq 0.25$ at r_{500} (Figure 2).

If we force $E_{\text{non-thermal}}/E_{\text{total}} \equiv 0$ throughout the cluster, we will obtain gas temperatures much higher than the observation in $\gtrsim r_{500}$ in some cases. As an example in Figure 3 we show the model predicted temperature profiles for the nine clusters discussed in §5.1 (light blue solid lines) when $E_{\text{non-thermal}}/E_{\text{total}} \equiv 0$ is set. In three clusters (A1835, A2142, and PKS 0745-191) the model profiles significantly deviate from the observed data, indicating that in these clusters the hydrostatic equilibrium is not well established in $0.45 - 1.5r_{500}$. For the rest six clusters, however, such a deviation is not seen in $r \leq r_{500}$ or even in $r \leq r_{200}$ within the error ranges. These results imply that for these clusters the assumption of hydrostatic equilibrium is safe at small and intermediate radii.

5.3. None Gravitational Interaction between Dark Matter and Baryonic Matter

The non-gravitational interactions between dark matter and luminous matter are expected to be very weak, therefore the kinetic energy of the dark matter can hardly be transferred to the hot gas. To test this we modify our model by adding a new free parameter f_{DMenergy} to describe the percentage of the dark matter’s kinetic energy that has been transferred to the gas. Assuming that the baryonic fraction of the total gravitating mass is 16%, the model temperature profile Eq. 16 is modified to be

$$T(r) = \frac{T_0 + (1 + (1/0.16 - 1)f_{\text{DMenergy}} - C_3)C_1\rho_0r_s^3 \ln((r_s + r)/r_s)/r}{1/\eta(r) - C_3 - C_2(K_{\text{obs}}(r) - K_{\text{model}}(r))/K_{\text{obs}}(r)}. \quad (19)$$

We find that f_{DMenergy} given by the fittings are consistent with zero for all clusters within the computational accuracy. This is accordant with the measurement results by astronomical

simulation (Munoz et al. 2015) and particle physics experiments (Aprile et al. 2012), which in turn verify the model.

6. SUMMARY

We investigate the gas temperature profiles in a sample of 50 clusters observed with *Chandra* by introducing a new temperature profile model, which takes into account the effects of both the gravitational heating, thermal history (such as radiative cooling, AGN feedback, and thermal conduction) and work done via gas compression, and use it to fit the observed temperature profiles by running Bayesian regressions. In all cases our model can provide an acceptable fit at the 68% confidence level. Also we find that by extrapolating the best-fit *Chandra* temperature profiles derived with our model to $1.5r_{500}$ the results agree very well with the *Suzaku* measurements. With the new model we show that for most clusters assumption of hydrostatic equilibrium is safe out to at least $0.5r_{500}$.

This work was supported by the Ministry of Science and Technology of China (grant No. 2013CB837900), the National Science Foundation of China (grant Nos. 11125313, 11203017, 11433002, 61271349, and 61371147), the Chinese Academy of Sciences (grant No. KJZD-EW-T01), Science and Technology Commission of Shanghai Municipality (grant No. 11DZ2260700), and Shanghai Key Lab for Particle Physics and Cosmology (SKLPPC) (Grant No. 11DZ2260700).

Table 1. Basic information of sample members^a

Name	Obsid	RA	DEC	Redshift
2PIGGJ0011.5-2850	5797	00:11:21.618	-28:51:21.47	0.0625
3C295	2254	14:11:20.676	+52:12:08.99	0.4641
3C388	5295	18:44:02.014	+45:33:30.68	0.0917
A1132	13376	10:58:26.518	+56:47:35.34	0.1363
A115N	13458	00:55:50.691	+26:24:37.25	0.1971
A115S	13458	00:55:59.283	+26:19:56.58	0.1971
A1201	9616	11:12:54.450	+13:26:00.44	0.1688
A1423	11724	11:57:17.344	+33:36:40.75	0.213
A1553	12254	12:30:46.941	+10:33:17.65	0.1652
A1664	7901	13:03:42.370	-24:14:43.66	0.1283
A1763	3591	13:35:18.357	+40:59:58.65	0.223
A1835	6880	14:01:01.971	+02:52:40.88	0.2532
A2061	10449	15:21:10.711	+30:37:58.27	0.0784
A2163	1653	16:15:46.098	-06:08:55.13	0.203
A2204	7940	16:32:46.981	+05:34:31.87	0.1522
A2218	1666	16:35:51.863	+66:12:37.99	0.1756
A2219	896	16:40:20.250	+46:42:30.65	0.2256
A2244	4179	17:02:42.316	+34:03:34.27	0.0968
A2249	12284	17:09:44.399	+34:27:24.18	0.0816
A2255	894	17:12:44.779	+64:04:29.86	0.0806
A2384	4202	21:52:21.450	-19:32:54.93	0.0943
A2409	3247	22:00:52.915	+20:58:27.42	0.1479
A2420	8271	22:10:19.165	-12:10:17.82	0.0846
A2457	12276	22:35:41.641	+01:29:11.35	0.0594
A2537	9372	23:08:22.105	-02:11:29.34	0.295
A2667	2214	23:51:39.337	-26:05:03.22	0.23
A3088	9414	03:07:01.858	-28:39:55.57	0.2534
A3158	3712	03:42:51.735	-53:37:48.13	0.0597
A3528	8268	12:54:40.759	-29:13:40.15	0.0530
A3695	12274	20:34:47.434	-35:49:03.38	0.0894
A3827	7920	22:01:53.464	-59:56:46.05	0.0984
A3921	4973	22:49:57.612	-64:23:43.40	0.0928

Table 1—Continued

Name	Obsid	RA	DEC	Redshift
A399	3230	02:57:51.172	+13:02:37.12	0.0718
A520	4215	04:54:09.806	+02:55:23.41	0.199
A644	2211	08:17:25.497	-07:30:39.40	0.0704
A665	13201	08:30:59.962	+65:50:35.49	0.1819
A773	5006	09:17:52.853	+51:43:39.91	0.217
MACSJ0035.4-2015	3262	00:35:26.339	-20:15:47.37	0.364
MACSJ1206.2-0847	3277	12:06:12.482	-08:48:05.73	0.44
MS0906.5+1110	924	09:09:12.615	+10:58:32.37	0.18
RXCJ0528.9-3927	4994	05:28:52.801	-39:28:21.11	0.2839
RXCJ0605.8-3518	15315	06:05:53.977	-35:18:08.60	0.141
RXCJ0638.7-5358	9420	06:38:47.101	-53:58:28.78	0.2216
RXCJ1329.7-3136	4165	13:29:47.398	-31:36:19.58	0.0495
RXCJ1504.1-0248	5793	15:04:07.630	-02:48:15.95	0.2153
RXCJ2218.6-3853	15101	22:18:39.634	-38:53:56.35	0.1379
RXJ0006.3+1052	12251	00:06:20.557	+10:51:52.98	0.1675
RXJ0439.0+0715	3583	04:39:00.678	+07:16:03.98	0.23
RXJ1023.7+0411	909	10:23:39.648	+04:11:11.90	0.2906
RXJ1720.1+2638	4361	17:20:10.115	+26:37:29.61	0.164

^aRight ascension and declination are in J2000.0.

Table 2. Average gas temperature, r_{500} , total gravitating mass and 0.5-10 keV luminosity within r_{500} , and model efficiency

Name	Average temperature ^a (keV)	M_{500} ($10^{14} M_{\odot}$)	r_{500} (kpc)	$L_{X,500}(0.5 - 10 \text{ keV})$ ($10^{44} \text{ erg s}^{-1}$)	R_{eff}
2PIGGJ0011.5-2850	$4.04^{+0.18}_{-0.18}$	$2.34^{+0.91}_{-0.51}$	913^{+106}_{-72}	1.93 ± 0.19	-0.37
3C295	$6.98^{+0.90}_{-0.72}$	$3.48^{+0.74}_{-0.52}$	910^{+60}_{-48}	11.0 ± 0.7	-0.17
3C388	$3.08^{+0.11}_{-0.21}$	$1.06^{+0.39}_{-0.20}$	694^{+76}_{-46}	0.70 ± 0.08	-0.33
A1132	$10.2^{+1.2}_{-1.1}$	$11.0^{+2.7}_{-2.2}$	1494^{+114}_{-107}	11.3 ± 0.9	0.33
A115N	$10.2^{+0.5}_{-0.5}$	$6.36^{+1.31}_{-1.36}$	1221^{+79}_{-94}	8.91 ± 0.52	-0.77
A115S	$8.19^{+0.31}_{-0.3}$	$5.78^{+1.56}_{-1.36}$	1183^{+98}_{-101}	8.17 ± 0.47	0.18
A1201	$6.45^{+0.31}_{-0.31}$	$4.68^{+2.47}_{-1.64}$	1112^{+169}_{-149}	5.95 ± 0.70	-0.30
A1423	$7.48^{+0.75}_{-0.70}$	$2.03^{+0.60}_{-0.58}$	866^{+78}_{-92}	1.12 ± 0.15	-0.37
A1553	$7.74^{+0.71}_{-0.71}$	$7.97^{+1.96}_{-1.26}$	1330^{+101}_{-74}	7.35 ± 0.53	-0.16
A1664	$5.35^{+0.26}_{-0.20}$	$3.79^{+0.40}_{-0.38}$	1050^{+36}_{-38}	4.84 ± 0.32	-0.63
A1763	$9.42^{+0.82}_{-0.82}$	$5.18^{+1.23}_{-0.80}$	1131^{+83}_{-61}	14.2 ± 0.9	-0.03
A1835	$11.5^{+0.6}_{-0.6}$	$10.8^{+1.1}_{-0.9}$	1430^{+47}_{-41}	37.7 ± 2.2	-0.97
A2061	$5.05^{+0.17}_{-0.17}$	$3.63^{+1.73}_{-0.51}$	1051^{+146}_{-51}	2.32 ± 0.21	0.45
A2163	$16.1^{+0.5}_{-0.5}$	$19.5^{+2.1}_{-2.5}$	1770^{+61}_{-79}	49.8 ± 2.8	0.19
A2204	$9.52^{+0.31}_{-0.31}$	$8.62^{+0.48}_{-0.41}$	1371^{+25}_{-22}	27.3 ± 1.5	-0.42
A2218	$7.11^{+0.38}_{-0.37}$	$6.50^{+0.39}_{-0.31}$	1239^{+24}_{-20}	9.52 ± 0.57	-0.07
A2219	$12.7^{+0.6}_{-0.7}$	$21.3^{+3.4}_{-4.3}$	1810^{+93}_{-131}	34.1 ± 2.0	0.08
A2244	$6.15^{+0.14}_{-0.14}$	$4.12^{+0.4}_{-0.6}$	1090^{+34}_{-54}	8.51 ± 0.51	-0.88
A2249	$6.98^{+0.66}_{-0.44}$	$4.03^{+5.17}_{-1.14}$	1087^{+344}_{-114}	3.22 ± 0.51	-0.12
A2255	$6.64^{+0.14}_{-0.14}$	$4.23^{+0.81}_{-0.48}$	1105^{+66}_{-44}	4.50 ± 1.28	-1.23
A2384	$5.85^{+0.27}_{-0.27}$	$2.77^{+0.26}_{-0.35}$	956^{+29}_{-42}	2.50 ± 0.19	-0.37
A2409	$6.52^{+0.45}_{-0.45}$	$6.20^{+1.68}_{-1.14}$	1230^{+102}_{-81}	9.52 ± 0.65	-0.32
A2420	$4.36^{+0.38}_{-0.29}$	$3.73^{+1.55}_{-0.83}$	1058^{+130}_{-86}	4.86 ± 0.51	0.20
A2457	$3.92^{+0.26}_{-0.27}$	$2.76^{+2.12}_{-1.05}$	965^{+193}_{-150}	1.05 ± 0.08	0.02
A2537	$8.84^{+1.24}_{-0.97}$	$4.30^{+0.92}_{-0.37}$	1036^{+67}_{-32}	9.94 ± 0.64	0.04
A2667	$7.97^{+0.89}_{-0.74}$	$6.51^{+2.52}_{-1.74}$	1217^{+140}_{-120}	24.9 ± 1.6	-0.33
A3088	$8.05^{+1.12}_{-0.78}$	$5.49^{+2.06}_{-0.81}$	1141^{+128}_{-59}	13.4 ± 1.0	0.42
A3158	$4.96^{+0.88}_{-0.88}$	$3.22^{+0.50}_{-0.37}$	1016^{+49}_{-41}	4.66 ± 0.42	-0.23
A3528	$5.03^{+0.34}_{-0.34}$	$2.18^{+0.62}_{-0.41}$	893^{+75}_{-61}	1.61 ± 0.15	0.12
A3695	$6.47^{+0.41}_{-0.41}$	$4.10^{+2.40}_{-1.84}$	1091^{+181}_{-197}	5.05 ± 0.55	0.14
A3827	$7.61^{+0.21}_{-0.21}$	$4.53^{+0.34}_{-0.28}$	1124^{+28}_{-23}	9.76 ± 0.63	0.03

Table 2—Continued

Name	Average temperature ^a (keV)	M_{500} ($10^{14} M_{\odot}$)	r_{500} (kpc)	$L_{X,500}(0.5 - 10 \text{ keV})$ ($10^{44} \text{ erg s}^{-1}$)	R_{eff}
A3921	$5.92^{+0.22}_{-0.22}$	$4.02^{+0.73}_{-0.37}$	1083^{+62}_{-34}	4.57 ± 0.31	-0.63
A399	$8.18^{+0.25}_{-0.25}$	$4.67^{+1.46}_{-0.79}$	1145^{+108}_{-72}	5.76 ± 0.37	0.13
A520	$9.04^{+0.80}_{-0.80}$	$6.78^{+0.74}_{-0.48}$	1246^{+44}_{-30}	13.2 ± 0.72	-0.10
A644	$8.28^{+0.21}_{-0.21}$	$6.70^{+0.37}_{-0.58}$	1292^{+23}_{-39}	9.10 ± 0.59	-0.06
A665	$12.2^{+0.7}_{-0.8}$	$7.65^{+1.90}_{-2.25}$	1305^{+100}_{-143}	16.1 ± 1.0	-0.26
A773	$7.67^{+0.60}_{-0.59}$	$5.26^{+3.72}_{-1.20}$	1139^{+222}_{-95}	11.0 ± 0.9	0.33
MACSJ0035.4-2015	$6.45^{+0.55}_{-0.46}$	$5.41^{+0.81}_{-1.01}$	1093^{+52}_{-72}	22.2 ± 1.6	0.36
MACSJ1206.2-0847	$15.8^{+2.5}_{-2.1}$	$11.7^{+3.7}_{-2.9}$	1374^{+132}_{-123}	41.5 ± 2.4	0.39
MS0906.5+1110	$5.46^{+0.42}_{-0.35}$	$4.09^{+0.48}_{-0.30}$	1059^{+53}_{-27}	5.98 ± 0.39	-0.06
RXCJ0528.9-3927	$9.08^{+1.18}_{-0.90}$	$8.18^{+2.48}_{-3.79}$	1290^{+119}_{-241}	19.4 ± 1.5	0.17
RXCJ0605.8-3518	$6.64^{+0.64}_{-0.50}$	$3.91^{+1.78}_{-0.64}$	1057^{+141}_{-61}	8.55 ± 0.74	-0.35
RXCJ0638.7-5358	$9.73^{+0.81}_{-0.81}$	$7.53^{+3.27}_{-2.02}$	1281^{+164}_{-126}	23.3 ± 1.4	0.02
RXCJ1329.7-3136	$3.45^{+0.17}_{-0.14}$	$0.79^{+0.22}_{-0.12}$	637^{+56}_{-35}	0.88 ± 0.06	-1.27
RXCJ1504.1-0248	$11.0^{+1.1}_{-0.8}$	$9.29^{+0.62}_{-0.48}$	1378^{+30}_{-25}	47.4 ± 2.7	-0.16
RXCJ2218.6-3853	$8.67^{+1.38}_{-0.9}$	$9.36^{+4.37}_{-2.00}$	1415^{+193}_{-109}	9.15 ± 0.54	0.40
RXJ0006.3+1052	$6.85^{+0.53}_{-0.36}$	$2.83^{+0.28}_{-0.41}$	941^{+30}_{-48}	4.87 ± 0.41	-1.28
RXJ0439.0+0715	$6.51^{+0.52}_{-0.42}$	$4.34^{+1.15}_{-0.61}$	1064^{+87}_{-52}	12.9 ± 0.9	-0.40
RXJ1023.7+0411	$9.26^{+0.62}_{-0.61}$	$6.64^{+0.97}_{-0.55}$	1200^{+56}_{-34}	35.4 ± 2.0	-0.04
RXJ1720.1+2638	$8.38^{+0.62}_{-0.49}$	$6.22^{+0.62}_{-0.76}$	1225^{+38}_{-57}	15.5 ± 0.95	-0.02

^aAverage temperature is calculated for $0.2 - 0.5r_{500}$ region.

Table 3. Nine clusters selected to compare our model predictions with the *Suzaku* measurements^a

Name	Obsid	RA	DEC	Redshift	Reference ^b
A1413	5003	11:55:18.168	+23:24:24.49	0.1427	Hoshino et al. 2010
A1689	6930	13:11:29.472	-01:20:30.12	0.183	Kawaharada et al. 2010
A1795	10898	13:48:52.742	+26:35:27.63	0.0625	Bautz et al. 2009
A1835	6880	14:01:01.971	+02:52:40.88	0.2532	Ichikawa et al. 2013
A2029	4977	15:10:56.195	+05:44:43.36	0.07728	Walker et al. 2012a
A2142	5005	15:58:19.972	+27:13:58.50	0.0909	Akamatsu et al. 2011
A2204	7940	16:32:46.981	+05:34:31.87	0.1522	Reiprich et al. 2009
A780	575	09:18:05.352	-12:05:46.55	0.0539	Sato et al. 2012
PKS 0745-191	6103	07:47:31.430	-19:17:42.29	0.1028	Walker et al. 2012b

^aRight ascension and declination are in J2000.0.

^b90% errors quoted from the references, except for A2029 and RXJ0747.5-1917, for which the errors are quote at the 68% confidence level. The projection effect are not corrected expect for A2029 and PKS 0745-191.

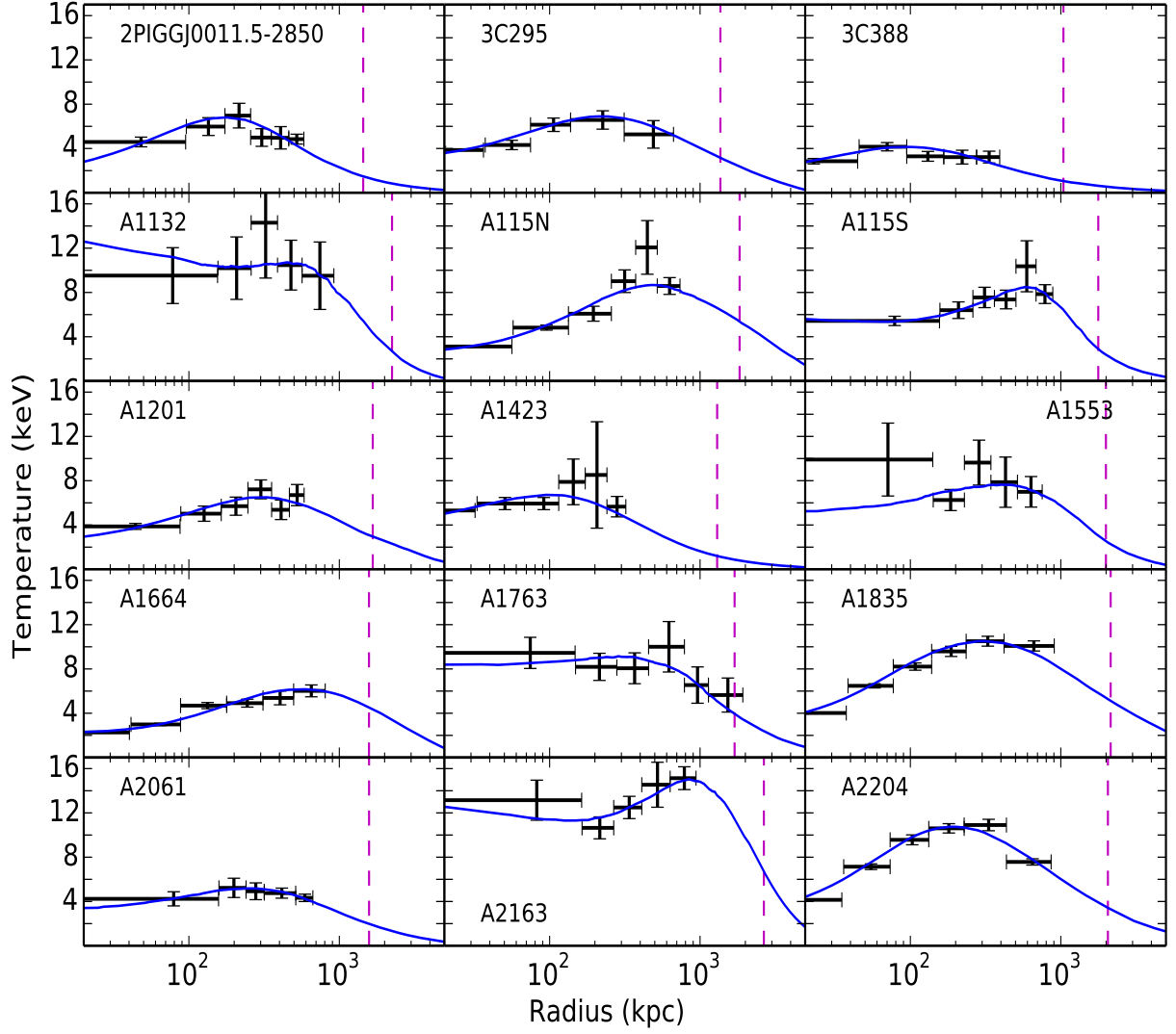


Fig. 1.— Best-fit gas temperature profiles obtained with our model (dark blue curves), along with the 68% errors (shadow), to the *Chandra* measurements (black crosses) after the projection effect is corrected (§3.2). The vertical dashed lines indicate $1.5r_{500}$ of each cluster.

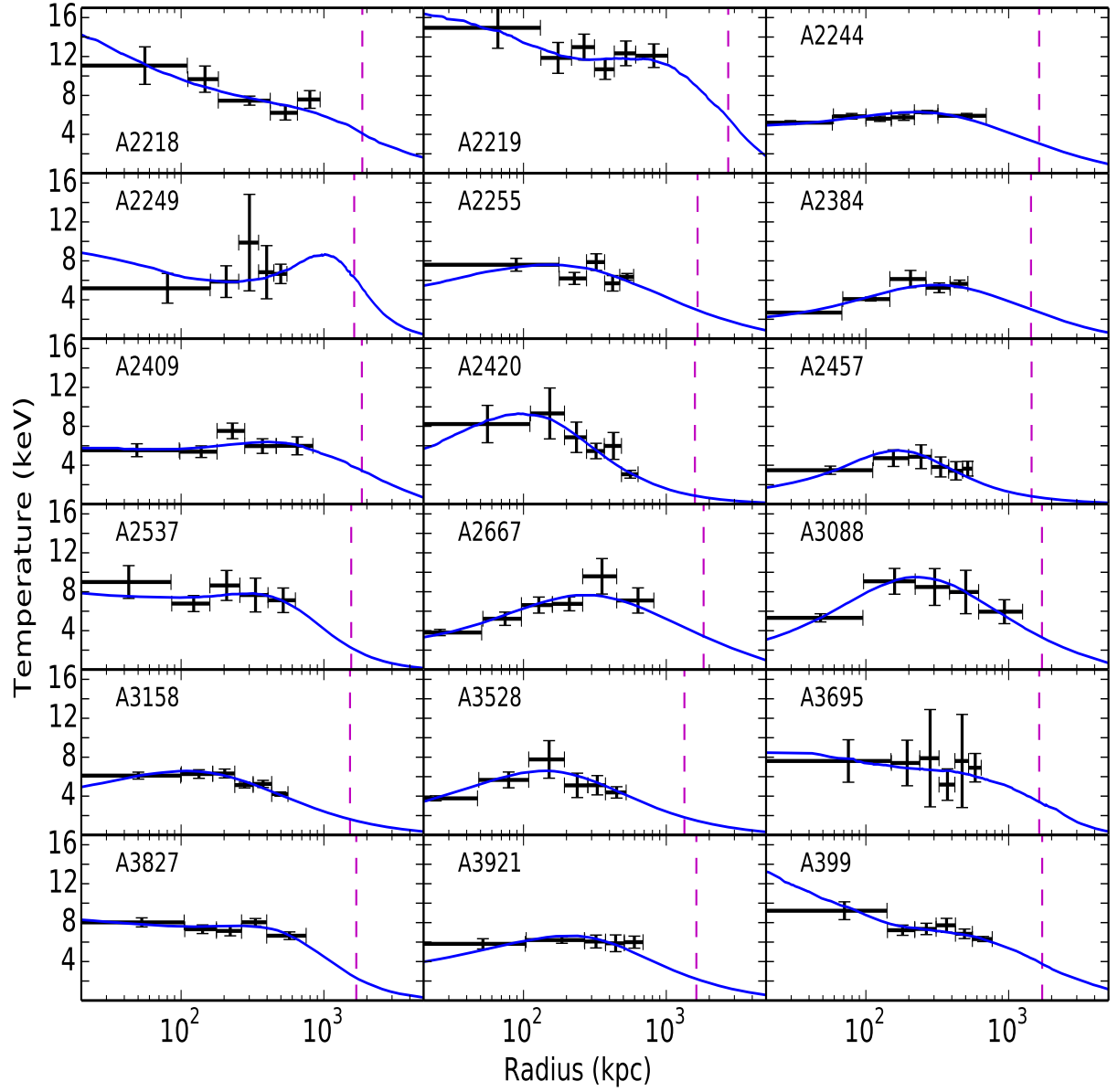


Fig. 1.— Fitting Result Continued

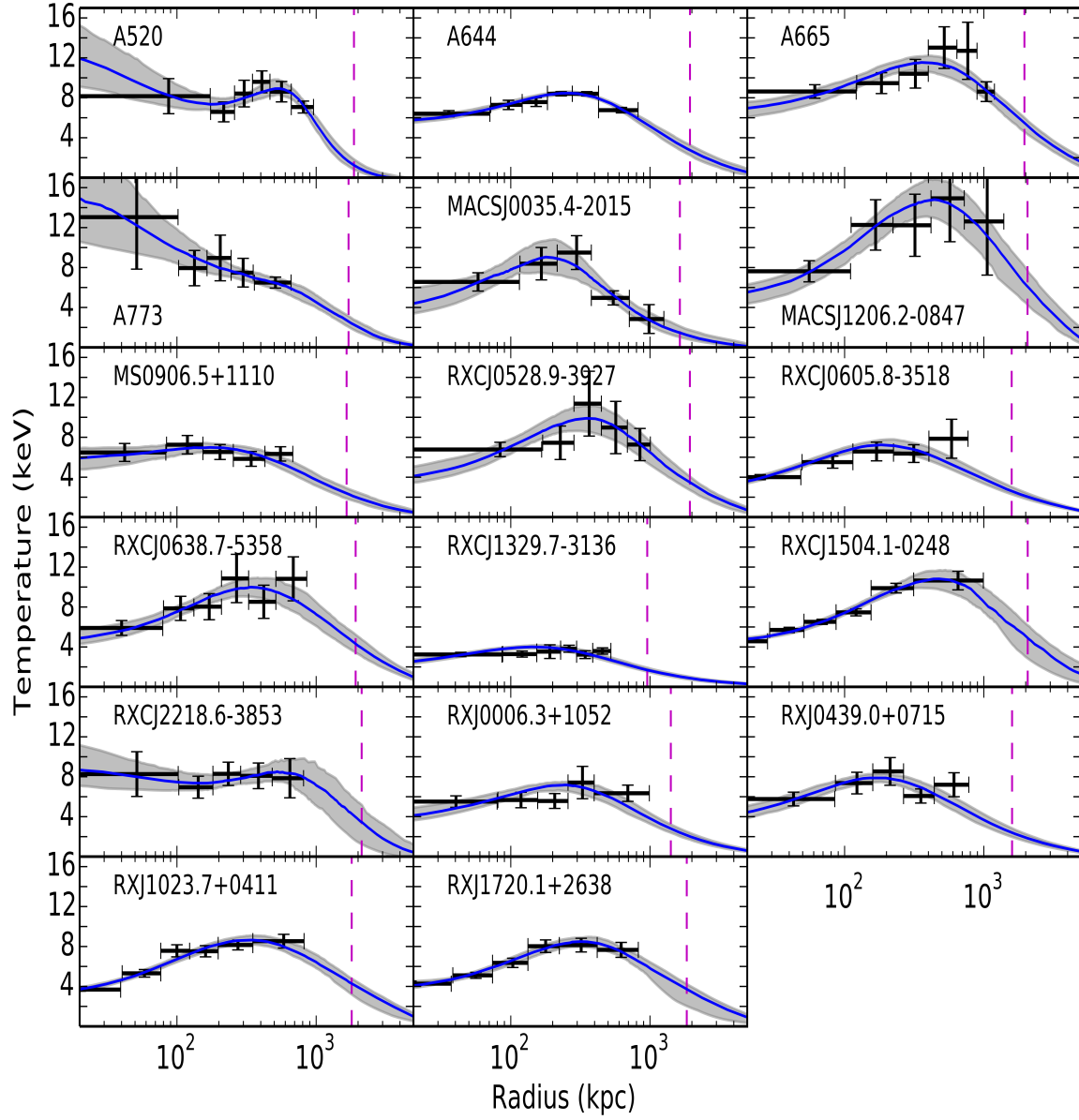


Fig. 1.— Fitting Result Continued

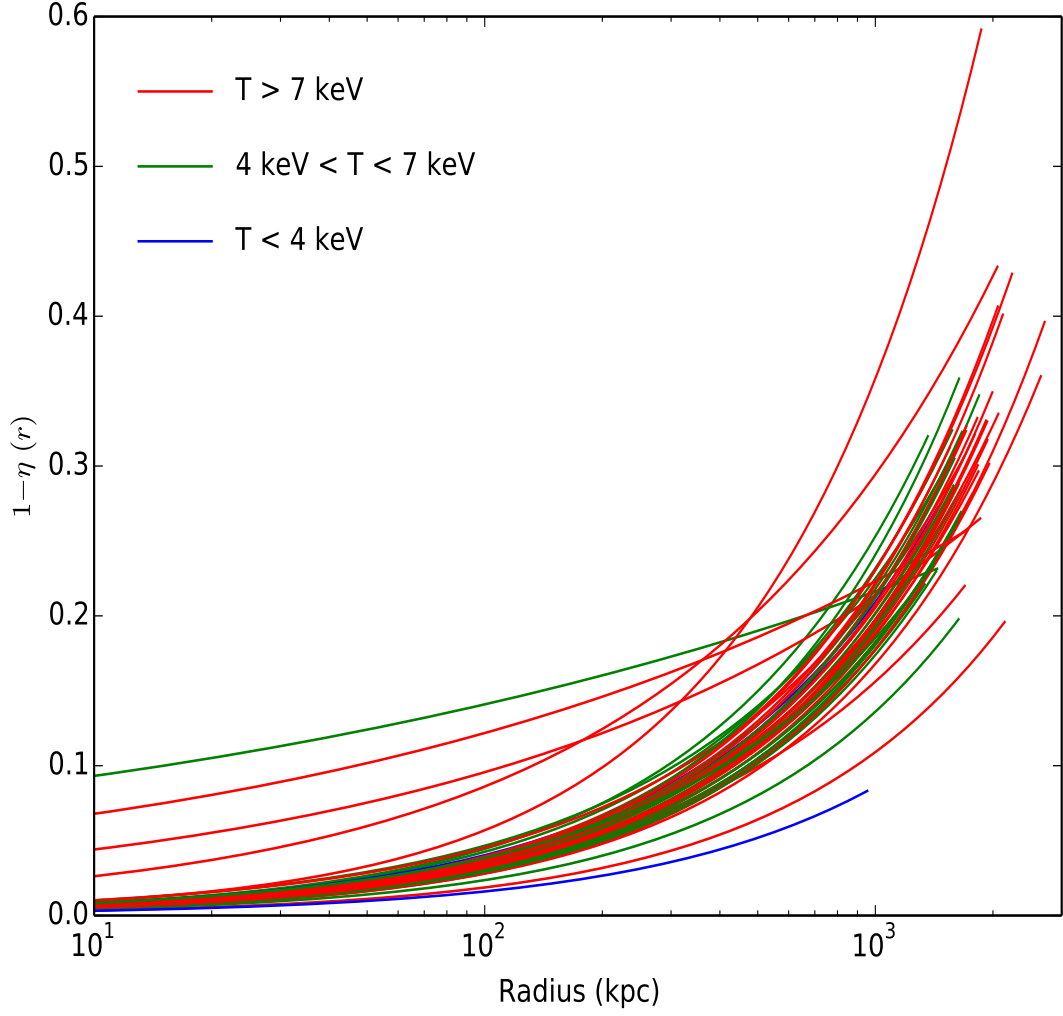


Fig. 2.— Non-thermal energy fraction $1 - \eta(r)$ (c.f., Eq. 14) as an index of the violation to the hydrostatic equilibrium, which are plotted out to $1.5r_{500}$, the radius cut used to compare between *Chandra* and *Suzaku* results. T in the legend stands for average temperature (Table 2) of the cluster.

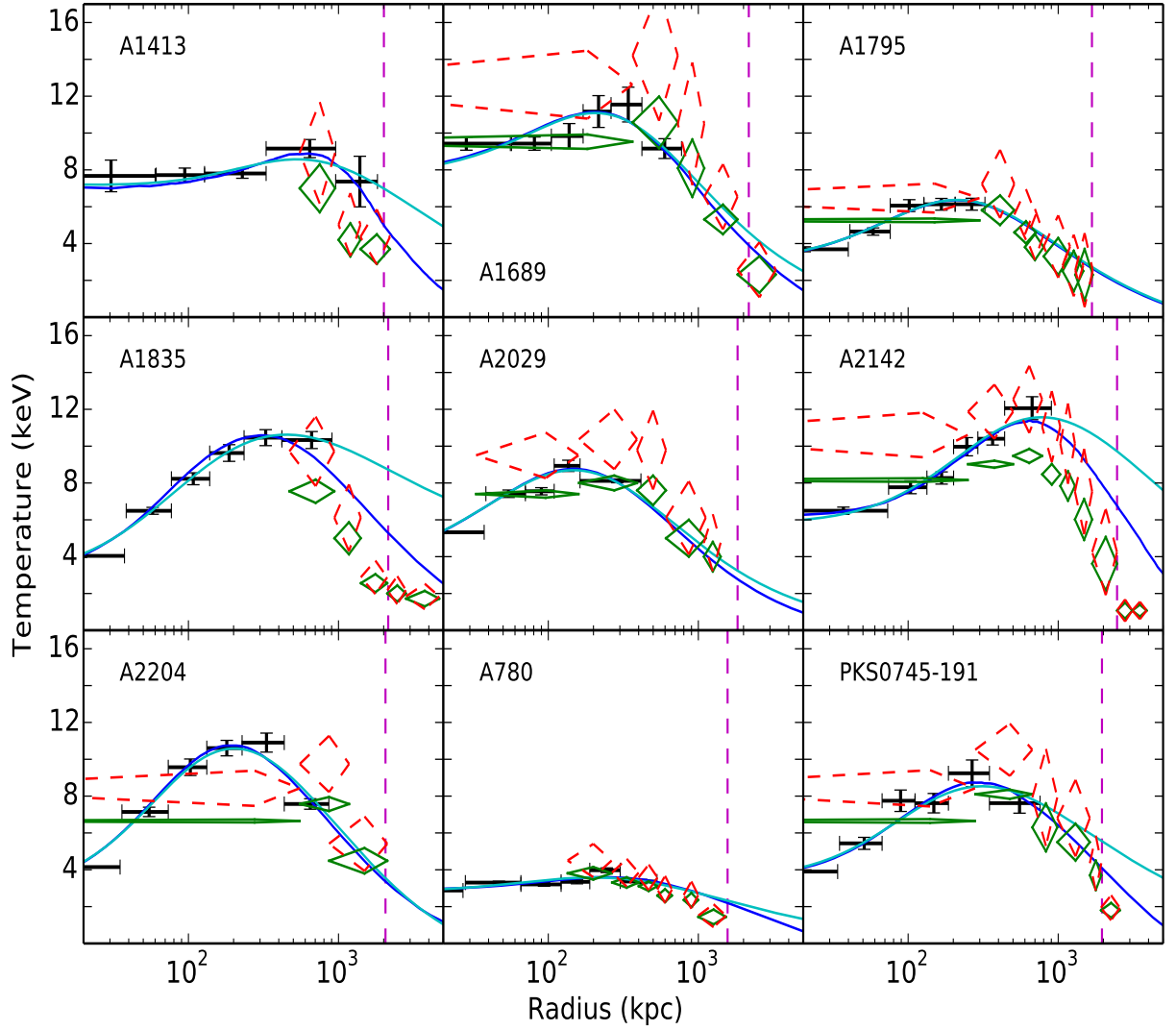


Fig. 3.— A comparison between the predictions of our model (dark blue curves), which are obtained based on the *Chandra* observation (dark crosses) along with the 68% errors (shadow), and the *Suzaku* measurements (original data are marked with green diamonds, and the data obtained after the differences between *Suzaku* and *Chandra* measurements are corrected are marked with red diamonds) out to $1.5r_{500}$, which are marked with dashed lines in magenta. The light blue curves show the model predictions when the assumption of hydrostatic equilibrium is forced throughout the cluster.

REFERENCES

- Akamatsu, H., Hoshino, A., Ishisaki, Y., et al. 2011, PASJ, 63, 1019
- Allen, S. W., Schmidt, R. W., & Fabian, A. C. 2001, MNRAS, 328, L37
- Andreon, S. 2012, A&A, 546, A6
- Andreon, S., & Hurn, M. A. 2012, Statistical Analysis and Data Mining: The ASA Data Science Journal, 6(1), 15-33.
- Aprile, E., Alfonsi, M., Arisaka, K., et al. 2012, Physical Review Letters, 109, 181301
- Arnaud K. A., 1996, in Jacoby G. H., Barnes J., eds, Astronomical Data Analysis Software and Systems V Vol. 101 of Astronomical Society of the Pacific Conference Series, XSPEC: The First Ten Years.
- Ascasibar, Y., & Markevitch, M. 2006, ApJ, 650, 102
- Battaglia, N., Bond, J. R., Pfrommer, C., & Sievers, J. L. 2012, ApJ, 758, 74
- Bautz, M. W., Miller, E. D., Sanders, J. S., et al. 2009, PASJ, 61, 1117
- Carter, J. A., & Read, A. M. 2007, A&A, 464, 1155
- Chaudhuri, A., Nath, B. B., & Majumdar, S. 2012, ApJ, 759, 87
- Dickey, J. M., & Lockman, F. J. 1990, ARA&A, 28, 215
- Engeland, K., & Gottschalk, L. 2002, Hydrology and Earth System Sciences, 6, 883
- Gastaldello, F., Buote, D. A., Humphrey, P. J., et al. 2007, ApJ, 669, 158
- Grevesse, N., & Sauval, A. J. 1998, Space Sci. Rev., 85, 161
- Gu, L., Xu, H., Gu, J., et al. 2012, ApJ, 749, 186

- Hoshino, A., Henry, J. P., Sato, K., et al. 2010, PASJ, 62, 371
- Humphrey, P. J., & Buote, D. A. 2006, ApJ, 639, 136
- Ichikawa, K., Matsushita, K., Okabe, N., et al. 2013, ApJ, 766, 90
- Kalberla, P. M. W., Burton, W. B., Hartmann, D., et al. 2005, A&A, 440, 775
- Kawaharada, M., Okabe, N., Umetsu, K., et al. 2010, ApJ, 714, 423
- Kettula, K., Nevalainen, J., & Miller, E. D. 2013, A&A, 552, A47
- Kravtsov, A. V., & Borgani, S. 2012, ARA&A, 50, 353
- Kushino, A., Ishisaki, Y., Morita, U., et al. 2002, PASJ, 54, 327
- Lin, H. W., McDonald, M., Benson, B., & Miller, E. 2015, ApJ, 802, 34
- Makishima, K., Ezawa, H., Fukuzawa, Y., et al. 2001, PASJ, 53, 401
- Meneghetti, M., Rasia, E., Merten, J., et al. 2010, A&A, 514, A93
- Munoz, J. B., Kovetz, E. D., & Ali-Haïmoud, Y. 2015, arXiv:1509.00029
- Mushotzky, R. F., Cowie, L. L., Barger, A. J., & Arnaud, K. A. 2000, Nature, 404, 459
- Nash, J. E., & Sutcliffe, J. V. 1970, Journal of Hydrology, 10, 282
- Navarro, J. F., Frenk, C. S., & White, S. D. M. 1996, ApJ, 462, 563
- Nevalainen, J., David, L., & Guainazzi, M. 2010, A&A, 523, A22
- Powell, M. J. 1964, The Computer Journal, 7(2), 155-162
- Panagoulia, E. K., Fabian, A. C., & Sanders, J. S. 2014, MNRAS, 438, 2341
- Reiprich, T. H., Hudson, D. S., Zhang, Y.-Y., et al. 2009, A&A, 501, 899

- Sato, T., Sasaki, T., Matsushita, K., et al. 2012, PASJ, 64, 95
- Schellenberger, G., Reiprich, T. H., Lovisari, L., Nevalainen, J., & David, L. 2015, A&A, 575, A30
- Smith, R. K., Brickhouse, N. S., Liedahl, D. A., & Raymond, J. C. 2001, ApJ, 556, L91
- Sun, M., Voit, G. M., Donahue, M., et al. 2009, ApJ, 693, 1142
- Vikhlinin, A., Markevitch, M., Murray, S. S., et al. 2005, ApJ, 628, 655
- Vikhlinin, A., Kravtsov, A., Forman, W., et al. 2006, ApJ, 640, 691
- Voit, G. M. 2005a, Reviews of Modern Physics, 77, 207
- Voit, G. M., Kay, S. T., & Bryan, G. L. 2005b, MNRAS, 364, 909
- Walker, S. A., Fabian, A. C., Sanders, J. S., George, M. R., & Tawara, Y. 2012a, MNRAS, 422, 3503
- Walker, S. A., Fabian, A. C., Sanders, J. S., & George, M. R. 2012b, MNRAS, 424, 1826
- Xu, H., Jin, G., & Wu, X.-P. 2001, ApJ, 553, 78
- Zhang, Y.-Y., Böhringer, H., Finoguenov, A., et al. 2006, A&A, 456, 55